

# Best-Buddy GANs for Highly Detailed Image Super-Resolution

Wenbo Li<sup>1\*</sup> Kun Zhou<sup>2\*</sup> Lu Qi<sup>1</sup> Liying Lu<sup>1</sup> Nianjuan Jiang<sup>2</sup> Jiangbo Lu<sup>2†</sup> Jiaya Jia<sup>1,2</sup>

<sup>1</sup>The Chinese University of Hong Kong <sup>2</sup>Smartmore Corporation

{wenboli, luqi, lylu, leojia}@cse.cuhk.edu.hk

{kun.zhou, nianjuan.jiang, jiangbo}@smartmore.com

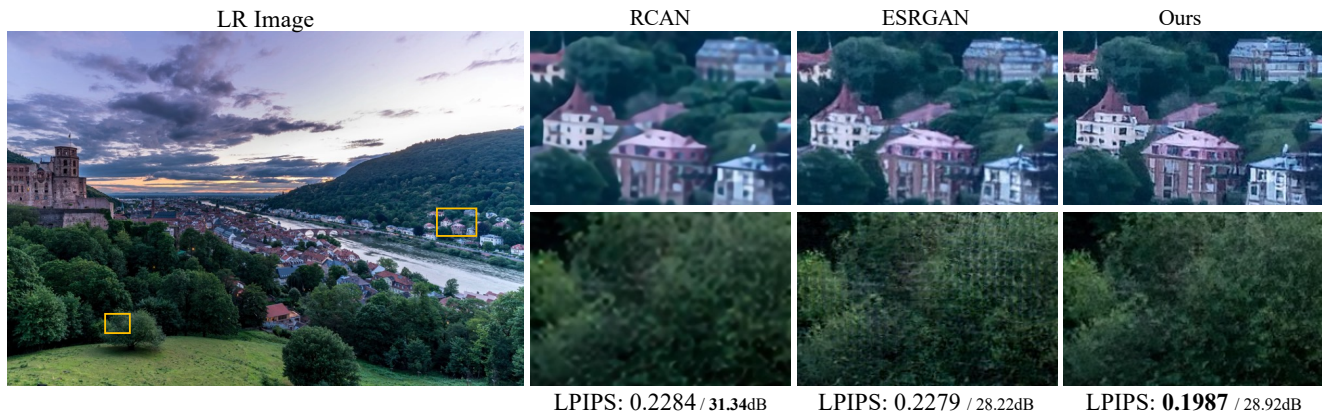


Figure 1: Visual comparison of our best-buddy GANs, PSNR-oriented RCAN [52] and perception-oriented ESRGAN [42]. The numbers are LPIPS(↓)/PSNR(↑). Richer details are generated in our result with much fewer artifacts.

## Abstract

We consider the single image super-resolution (SISR) problem, where a high-resolution (HR) image is generated based on a low-resolution (LR) input. Recently, generative adversarial networks (GANs) become popular to hallucinate details. Most methods along this line rely on a pre-defined single-LR-single-HR mapping, which is not flexible enough for the SISR task. Also, GAN-generated fake details may often undermine the realism of the whole image. We address these issues by proposing best-buddy GANs (BebyGAN) for rich-detail SISR. Relaxing the immutable one-to-one constraint, we allow the estimated patches to dynamically seek the best supervision during training, which is beneficial to producing more reasonable details. Besides, we propose a region-aware adversarial learning strategy that directs our model to focus on generating details for textured areas adaptively. Extensive experiments justify the effectiveness of our method. An ultra-high-resolution 4K dataset is also constructed to facilitate future super-resolution research.<sup>1</sup>

\*Equal contribution

†Corresponding author

<sup>1</sup>Please find a higher quality version of this paper at <https://github.com/Jia-Research-Lab/Simple-SR>.

## 1. Introduction

The increasing demand for high-quality displays has promoted the rapid development of single image super-resolution (SISR). SISR has been successfully applied to a wide range of tasks, such as medical diagnostic imaging, security imaging and satellite imaging.

A great number of methods were proposed based on insightful image priors and optimization techniques, such as self-similarity [29, 8, 45, 12] and sparsity [23, 47, 48, 49, 39, 30, 28]. In recent years, deep-learning-based methods [4, 16, 17, 32, 19, 36, 37, 22, 10, 53, 52] further advanced SISR. Most of them rely on an immutable one-to-one supervision to pursue high PSNR but possibly generate blurry results. For example, the solution of commonly adopted one-to-one MSE/MAE metric approximates mean or median of data [35]. As shown in Figure 1, the HR estimation of RCAN [52] achieves the highest PSNR, yet lacking high-frequency texture.

To enhance the perceptual quality of recovered images, several methods [14, 20, 26, 42, 51, 34] use adversarial learning and perceptual loss [14]. It is noted that the issue of excessive smoothing caused by the one-to-one MSE/MAE loss is still not optimally addressed. Besides, the training of generative adversarial networks (GANs) [9] could be unsta-

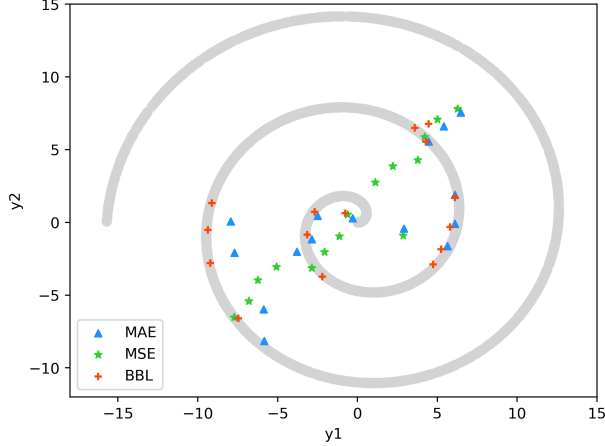


Figure 2: Toy example of **one-to-one** MAE, MSE and our **one-to-many** best-buddy loss (BBL) in SR. In training, two-dimensional HR data  $y = [y_1, y_2]$  is drawn from a Swiss-roll distribution (in gray). One-dimensional LR data is obtained by linearly downsampling HR data as  $x = \frac{y_1 + y_2}{2}$  like [35]. In testing, we plot the HR estimates of MAE ( $\blacktriangle$ ), MSE ( $\star$ ) and BBL ( $+$ ) for  $x \in [-7, -6, \dots, 7]$ . Our BBL fits the distribution best because it produces more HR estimates that fall on the roll.

ble and result in unpleasant visual artifacts (see the recovered tree of ESRGAN [42] in Figure 1). Thus in this paper, we aim to address these issues from two aspects.

It is well-known that SISR is essentially an ill-posed problem since a single low-resolution (LR) patch may correspond to multiple high-resolution (HR) solutions - it is difficult to decide the best. The commonly used one-to-one MSE/MAE loss tends to enforce a rigid mapping between the given LR-HR pair, which strictly constrains the HR space and makes it difficult to train the network. Relaxing the one-to-one constraint, we propose a novel *best-buddy loss*, an improved one-to-many MAE loss, to allow finding and using HR supervision signals flexibly by exploiting the ubiquitous self-similarity existing in natural images. Put it differently, an estimated HR patch is allowed to be supervised by different but close-to-ground-truth (GT) patches sourced from multiple scales of the corresponding GT image. From the toy example in Figure 2, it is noticeable that our best-buddy loss outperforms one-to-one MSE/MAE. Additionally, a back-projection constraint is adopted to ensure the validity of the estimated HR signal.

As aforementioned, undesirable artifacts may be produced in images for existing GAN-based methods [14, 20, 26, 42, 51, 34]. We propose a region-aware adversarial learning strategy to address it. Our network treats smooth and well-textured areas differently, and only performs the adversarial training on the latter. This separation encourages the network to focus more on regions with rich details while avoiding generating unnecessary texture on flat re-

gions (e.g., sky and building). With this improvement, our proposed best-buddy GANs (termed as *Beby-GAN*) is able to reconstruct photo-realistic high-frequencies with fewer undesirable artifacts (see Figure 1).

In summary, our contribution is threefold:

- We present Beby-GAN for high-quality image super-resolution. The proposed *one-to-many* best-buddy loss benefits generating richer and more plausible texture. Extensive experiments and a user study justify the effectiveness of the proposed method.
- A region-aware adversarial learning strategy is designed to further enhance the visual quality of images.
- Breaking through the 2K resolution limitation of current SISR datasets, we provide an ultra-high-resolution 4K (UH4K) image dataset with diverse categories to promote future research, which will be made publicly available.

## 2. Related Work

Single image super-resolution (SISR) is a classical image restoration task. It is roughly divided into three categories of example-based or prior-based methods [47, 8, 45, 49, 39, 30, 40], PSNR-oriented methods [4, 16, 17, 32, 19, 36, 37, 22, 10, 53, 52] and perception-driven methods [14, 20, 31, 26, 42, 43, 41, 51, 7, 34].

### 2.1. Example-Based Methods

This line [47, 49, 40, 46, 28] learns mapping from low-resolution patches to high-resolution counterparts, where the paired patches are collected from an external database. In this paper, we exploit this idea to search for one-to-many LR-HR mappings to produce visually pleasing results.

### 2.2. PSNR-Oriented Methods

In past years, particular attention is paid to improve the pixel-wise reconstruction measures (e.g., peak-to-noise ratio, PSNR). It is the first time that SRCNN [4] introduces a deep convolutional neural network into the SISR task. Afterwards, more well-designed architectures were proposed including residual and recursive learning [16, 17, 36, 22], sub-pixel upsampling [32], Laplacian pyramid structure [19] and dense connecting [53]. Especially, Zhang *et al.* [52] integrated channel attention modules into a network achieving a significant improvement in terms of PSNR performance. Hu *et al.* [11] proposed Meta-SR to enable a single network to upsample an image into arbitrary sizes. Hussein *et al.* [13] designed a closed-form correction filter to convert an unknown degraded image to a counterpart obtained from a standard bicubic kernel, and thus improved the generalization ability of pretrained models.

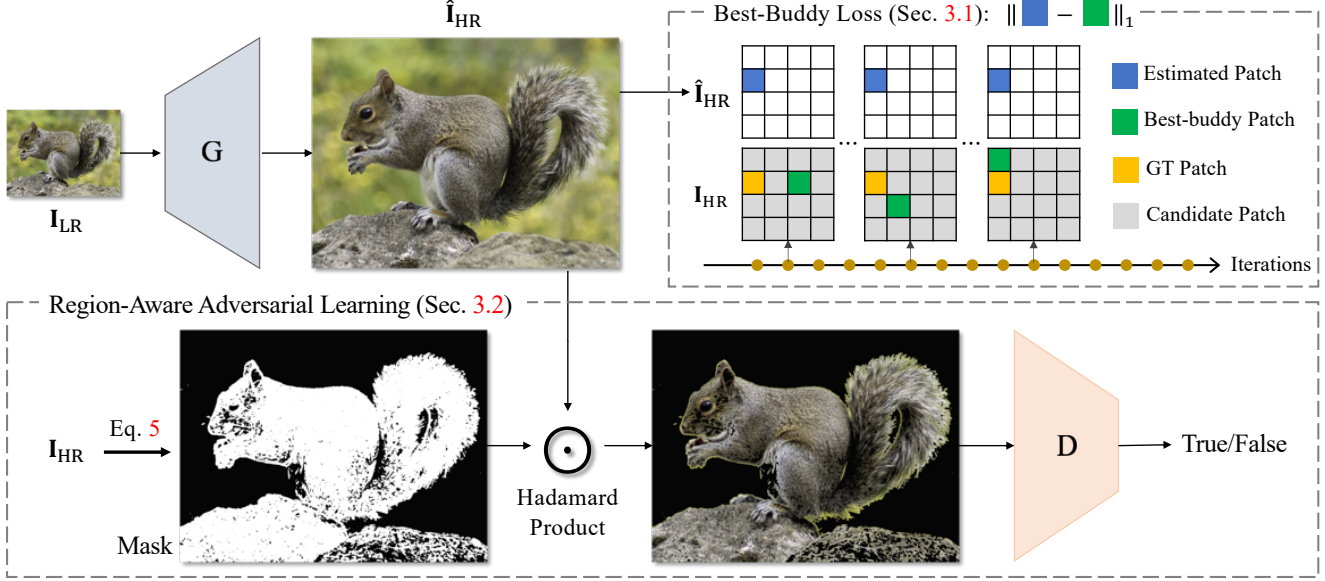


Figure 3: The framework of our proposed Beby-GAN. The best-buddy loss allows the estimated HR patches to be *optimally* supervised in a dynamic way during training, as detailed in Sec. 3.1 and Fig. 4(c). The region-aware adversarial learning is proposed to make the discriminator focus on rich-texture areas.

### 2.3. Perception-Driven Methods

Despite breakthroughs on PSNR, the aforementioned methods still face a challenge that super-resolved images are typically overly-smooth and lack high-frequencies. To tackle this problem, Johnson *et al.* [14] proposed a novel perceptual loss. Ledig *et al.* [20] presented SRGAN, which utilizes an adversarial loss and a content loss to push outputs into residing on the manifold of natural images. Thanks to a patch-wise texture loss, EnhanceNet [31] obtains better performance on both quantitative and qualitative evaluation. ESRGAN [42] marked a new milestone, which consistently generates more realistic texture benefiting from model and loss improvements. Later on, Zhang *et al.* [51] proposed RankSRGAN capable of being optimized towards a specific perceptual metric. In order to avoid undesirable artifacts, Soh *et al.* [34] introduced a naturalness prior to constrain the reconstructed image in the natural manifold. However, most of these methods rely on single-LR-single-HR MSE/MAE supervision. Besides, without a region-aware mechanism, the architecture design can not deal with regions differently according to their properties. From these perspectives, we propose best-buddy GANs detailed as follows.

### 3. Beby-GAN for Image Super-Resolution

Given a low-resolution (LR) image  $I_{LR} \in \mathbb{R}^{H \times W}$ , single image super-resolution (SISR) is supposed to generate a high-resolution (HR) counterpart  $\hat{I}_{HR} \in \mathbb{R}^{Hs \times Ws}$  under an upscale factor  $s$ . As shown in Figure 3, the main body of our framework is built upon the generative adversarial networks

(GANs) [9], where the generator is used to reconstruct high-resolution images and the discriminator is trained to distinguish between recovered results and real natural images. Following [42], we adopt a pretrained RRDB model as our generator since it has demonstrated strong learning ability. In this section, we first describe the proposed best-buddy loss and region-aware adversarial learning strategy, followed by explaining other loss functions.

#### 3.1. Best-Buddy Loss

In the super-resolution task, a single LR patch is essentially associated with multiple natural HR solutions, as illustrated in Figure 4(a). Existing methods generally focus on learning immutable single-LR-single-HR mapping using an MSE/MAE loss in the training phase (see Figure 4(b)), which ignores the inherent uncertainty of SISR. As a result, the reconstructed HR images may lack several high-frequency structures [24, 14, 5, 6, 20].

To alleviate this issue, we propose a one-to-many best-buddy loss to enable trustworthy but much more flexible supervision. The key idea is that an estimated HR patch is allowed to be supervised by diverse targets in different iterations (see Figure 3). In this paper, all supervision candidates come from a multi-scale ground-truth image pyramid. As shown in Figure 4(c), for an estimated HR patch  $\hat{p}_i$ , we look for its corresponding supervision patch  $g_i^*$  (i.e., *best buddy*) in the current iteration to meet two constraints:

**Constraint 1.**  $g_i^*$  is required to be close to the predefined ground-truth  $g_i$  in the HR space (1<sup>st</sup> term in Eq. 2). Relying on the ubiquitous multi-scale self-similarity in natural



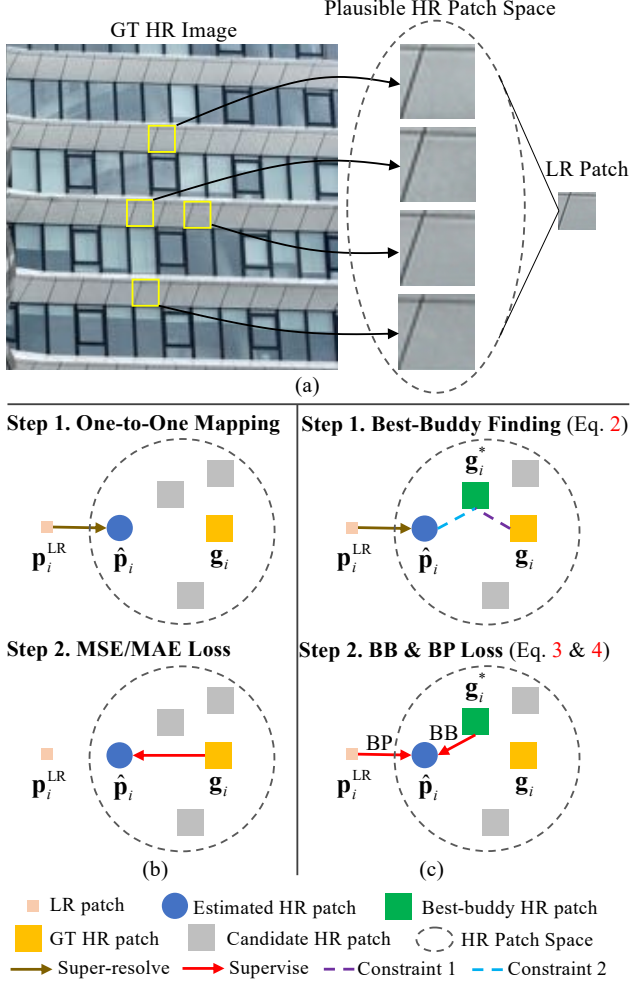


Figure 4: Comparison of the MSE/MAE and the best-buddy (BB) loss with a back-projection (BP) constraint. (a) Depiction of one-to-many nature in the SISR task. (b) MSE/MAE loss. (c) BB and BP loss. Variables  $p_i^{LR}$ ,  $\hat{p}_i$ ,  $g_i$  and  $g_i^*$  indicate the LR patch, estimated HR patch, ground-truth HR patch and best-buddy HR patch in current iteration.

images [18, 29, 8, 45, 12, 21], it is very likely to find a HR patch that is close to the ground-truth  $g_i$ .

**Constraint 2.** In order to make optimization easy,  $g_i^*$  ought to be close to the estimation  $\hat{p}_i$  ( $2^{nd}$  term in Eq. 2). Note that  $\hat{p}_i$  is considered to be a reasonable prediction as our generator is well initialized.

Optimized with these two objectives, the obtained best buddy  $g_i^*$  is regarded as a plausible HR target for supervision. In detail, we first downsample the ground-truth (GT) HR image  $I_{HR}$  with different scale factors as

$$I_{HR}^r = S(I_{HR}, r), \quad r = \{2, 4\}, \quad (1)$$

where  $S(I, r) : \mathbb{R}^{H \times W} \rightarrow \mathbb{R}^{\frac{H}{r} \times \frac{W}{r}}$  is a bicubic downsam-

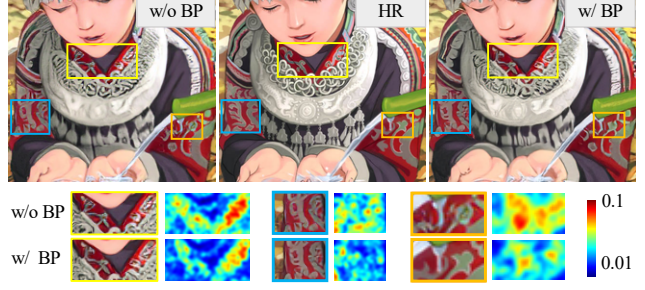


Figure 5: Comparison between with (w/) and without (w/o) the back-projection (BP) loss. We visualize the L2 error heatmaps between the estimated results and ground truth.

pling operator, and obtain a 3-level image pyramid (including the original GT HR image). Then, we unfold the estimated HR image and corresponding GT image pyramid into patches ( $3 \times 3$  in our paper), among which the GT part forms the supervision candidate database  $\mathcal{G}$  of this image. For the  $i$ -th estimated patch  $\hat{p}_i$ , instead of being supervised by the immutable predefined GT patch  $g_i$ , it is allowed to find the best buddy  $g_i^*$  in the current iteration as

$$g_i^* = \arg \min_{g \in \mathcal{G}} \alpha \|g - g_i\|_2^2 + \beta \|g - \hat{p}_i\|_2^2, \quad (2)$$

where  $\alpha \geq 0$  and  $\beta \geq 0$  are scaling parameters. The best-buddy loss for this patch pair  $(\hat{p}_i, g_i^*)$  is represented as

$$\mathcal{L}_{BB}(\hat{p}_i, g_i^*) = \|\hat{p}_i - g_i^*\|_1. \quad (3)$$

Notice that when  $\beta \ll \alpha$ , the proposed best-buddy loss degenerates into the typical one-to-one MAE loss.

Besides, we enforce another back-projection constraint on the estimation  $\hat{I}_{HR}$ . The super-resolved images after downscaling must match the fidelity expected at the lower resolution. We introduce an HR-to-LR operation (bicubic downsampling in this paper) to ensure that the projection of the estimated HR image onto the LR space is still consistent with the original LR one. The back-projected result is supervised by

$$\mathcal{L}_{BP} = \|S(\hat{I}_{HR}, s) - I_{LR}\|_1, \quad (4)$$

where  $s$  is the downscale factor. From Figure 5, we notice that this back-projection loss plays an essential role in maintaining content and color consistency.

### 3.2. Region-Aware Adversarial Learning

As shown in Figure 1, previous GAN-based methods sometimes produce undesirable texture, especially in flat regions. Thus, as illustrated in Figure 3, we propose to differentiate the rich-texture areas from smooth ones according to local pixel statistics, and only feed the textured content to the discriminator since smooth regions can be easily recovered without adversarial training. Our strategy is to first



unfold the ground-truth HR image (i.e.,  $\mathbf{I}_{\text{HR}} \in \mathbb{R}^{H \times W \times s}$ ) into patches  $\mathbf{B} \in \mathbb{R}^{H \times W \times s \times k^2}$  with size  $k^2$ , and then compute standard deviation (std) for each patch. After that, a binary mask is obtained as

$$\mathbf{M}_{i,j} = \begin{cases} 1, & \text{std}(\mathbf{B}_{i,j}) \geq \delta \\ 0, & \text{std}(\mathbf{B}_{i,j}) < \delta, \end{cases} \quad (5)$$

where  $\delta$  is a predefined threshold and  $(i, j)$  is the patch location. The highly textured regions are marked as 1 while flat regions as 0. Then the estimated result  $\hat{\mathbf{I}}_{\text{HR}}$  and ground-truth  $\mathbf{I}_{\text{HR}}$  are multiplied with the same mask  $\mathbf{M}$  yielding  $\hat{\mathbf{I}}_{\text{HR}}^{\mathbf{M}}$  and  $\mathbf{I}_{\text{HR}}^{\mathbf{M}}$ , which are next processed by the following discriminator. Though more sophisticated strategies can be used at the cost of more computation, we show that this simple masking method already works very well in Sec. 4.3. It directs our model to generate realistic fine details for textured areas.

### 3.3. Other Loss Functions

**Perceptual Loss.** Apart from computing pixel-wise distances in image space, several works [6, 5, 14] use feature similarity to enhance the perceptual quality of recovered images. Following this idea, we set the perceptual loss as

$$\mathcal{L}_{\text{P}} = \sum_i \eta_i \left\| \phi_i(\hat{\mathbf{I}}_{\text{HR}}) - \phi_i(\mathbf{I}_{\text{HR}}) \right\|_1, \quad (6)$$

where  $\phi_i$  represents the  $i$ -th layer activation of a pretrained VGG-19 [33] network and  $\eta_i$  is a scaling coefficient. To capture feature representations at different levels, we take into consideration three layers including  $\text{conv}_{3.4}$ ,  $\text{conv}_{4.4}$  and  $\text{conv}_{5.4}$  and set scaling coefficients to  $\frac{1}{8}$ ,  $\frac{1}{4}$  and  $\frac{1}{2}$ .

**Adversarial Loss.** The discriminator in our network is implemented based on Relativistic average GANs (RaGANs) [15], which estimate the probability that a ground-truth HR image is more realistic than a generated one. It has been shown that RaGANs are more stable and can produce results of higher quality [15, 42, 34]. The loss functions are formulated as

$$\mathcal{L}_{\text{D}} = -\mathbb{E}_{x_r \sim \mathbb{P}} [\log(\bar{D}(x_r))] - \mathbb{E}_{x_f \sim \mathbb{Q}} [\log(1 - \bar{D}(x_f))], \quad (7)$$

$$\mathcal{L}_{\text{G}} = -\mathbb{E}_{x_r \sim \mathbb{P}} [\log(1 - \bar{D}(x_r))] - \mathbb{E}_{x_f \sim \mathbb{Q}} [\log(\bar{D}(x_f))], \quad (8)$$

where

$$\bar{D}(x) = \begin{cases} \text{sigmoid}(C(x) - \mathbb{E}_{x_f \sim \mathbb{Q}} C(x_f)), & x \text{ is real} \\ \text{sigmoid}(C(x) - \mathbb{E}_{x_r \sim \mathbb{P}} C(x_r)), & x \text{ is fake.} \end{cases} \quad (9)$$

In Eq. 9,  $x_r$  denotes the masked real data sampled from distribution  $\mathbb{P}$ ,  $x_f$  is the masked fake data (i.e., generated data) sampled from distribution  $\mathbb{Q}$  and  $C(x)$  is the non-transformed discriminator output.



Figure 6: Visualization of examples from four categories in our proposed UH4K dataset.

**Overall Loss.** The overall loss of the generator is formulated as:

$$\mathcal{L} = \lambda_1 \mathcal{L}_{\text{BB}} + \lambda_2 \mathcal{L}_{\text{BP}} + \lambda_3 \mathcal{L}_{\text{P}} + \lambda_4 \mathcal{L}_{\text{G}}, \quad (10)$$

where  $\lambda_1 = 0.1$ ,  $\lambda_2 = 1.0$ ,  $\lambda_3 = 1.0$  and  $\lambda_4 = 0.005$ .

## 4. Experiments

### 4.1. Datasets and Metrics

Following previous methods [42, 51], our network is trained on DIV2K [1] (800 images) and Flickr2K [38] (2650 images) datasets. Apart from the widely used testing benchmark including Set5 [2], Set14 [49], BSDS100 [23] and Urban100 [12], we also adopt the 100 validation images in DIV2K to evaluate the performance of our model.

Besides, we propose an ultra-high-resolution 4K (UH4K) dataset to perform a more challenging and complete study on the single image super-resolution (SISR) task. The images are collected from YouTube with resolution  $3840 \times 2160$ . The dataset contains over 400 images featuring four categories, i.e., animal, city, nature and sports. A few examples are visualized in Figure 6. Compared with existing benchmark datasets, ours has higher resolution, higher variety and richer texture/structure. In this paper, our 4K dataset is *only* used for evaluation.

Apart from PSNR and SSIM [44] (the higher, the better ideally), we adopt a ground-truth-based perceptual metric LPIPS [50] and a no-reference perceptual metric PI [3] (the lower, the better ideally) in our experiments. Besides, we conduct a user study to make a better comparison.

### 4.2. Training Details

All experiments are carried out on NVIDIA GeForce RTX 2080 Ti GPUs under the  $\times 4$  setting. The mini-batch size is set to 8. We adopt Adam as the optimizer with  $\beta_1 = 0.9$  and  $\beta_2 = 0.999$ . There are 3 periods in our training, each with 200K iterations. The learning rate for every

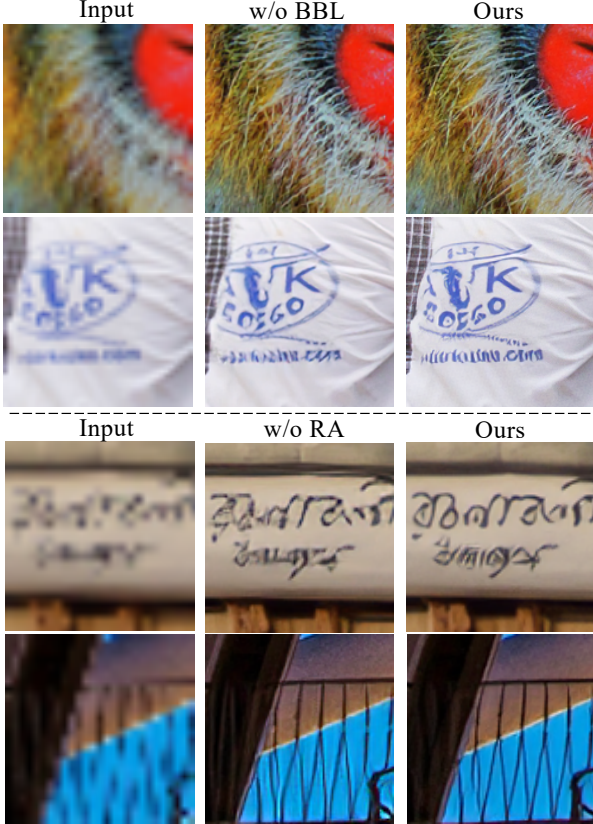


Figure 7: Visual comparison for ablation study. “Ours” is our proposed Beby-GAN. “w/o BBL” and “w/o RA” means removing best-buddy loss and region-aware learning.

period is set to  $1e^{-4}$  initially in accompany with a warm-up and a cosine decay. The images are augmented with random cropping, flipping and rotation. The input size is  $48 \times 48$  and the rotation is  $90^\circ$  or  $-90^\circ$ . The  $\alpha$  and  $\beta$  in Sec. 3.1 are both set to 1.0. The kernel size  $k$  and  $\delta$  in Sec. 3.2 are set to 11 and 0.025 (for normalized images) from empirical experiments. The calculation of best-buddy loss only costs 5.9ms for images of size  $196 \times 196$ .

### 4.3. Ablation Study

In this part, we investigate how each design affects the perceptual quality of super-resolved images. Starting from our best-buddy GANs (Beby-GAN), we ablate the best-buddy loss and region-aware learning strategy, respectively. We show a visual comparison in Figure 7. Also, we evaluate the LPIPS performance in Table 1 because the ground-truth-based LPIPS is more consistent with human perception compared with no-reference perceptual metrics illustrated in Sec. 4.4. All these results verify the effectiveness of our method.

**Best-buddy loss.** In contrast to the commonly used one-to-one MSE/MAE loss, our best-buddy loss allows the net-

Models	Ours	w/o BBL	w/o RA
Set14 [49]	<b>0.2202</b>	0.2343	0.2272
BSDS100 [23]	<b>0.2385</b>	0.2514	0.2469

Table 1: LPIPS comparison for ablation study. “Ours” is our proposed Beby-GAN. “w/o BBL” and “w/o RA” indicate removing best-buddy loss and region-aware learning.

work to learn single-LR-multiple-HR mapping. As illustrated in Figure 7, our BBL (see “Ours”) recovers richer texture and sharper edges compared with one-to-one MAE (see “w/o BBL”). The whiskers have more high-frequency details and the text is clearer. Also, we notice that the super-resolved images are more natural and visually pleasing. As shown in Table 1, the best-buddy loss brings about considerable improvement on LPIPS results.

**Region-Aware Adversarial Learning.** As shown in the Figure 7, there exist unpleasant artifacts near the characters and railing in the results without region-aware learning (see “w/o RA”). After differentiating between rich-texture and flat areas, this problem is alleviated as shown in the 3<sup>rd</sup> column (see “Ours”). The separation allows the network to know “where” to conduct the adversarial training and yields two major advantages. On the one hand, it leads to easier training since the network only needs to focus on regions of high-frequency details. On the other hand, the network produces less unnatural texture. The results in Table 1 also demonstrate the effectiveness of this strategy.

## 4.4. Comparison with State-of-the-Art Methods

We compare our Beby-GAN with start-of-the-art methods of two categories. They are PSNR-oriented methods including SRResNet [20], RRDB [42], RCAN [52], and perception-driven methods including ESRGAN [42] and RankSRGAN [51]. We use Set14 [49], BSDS100 [23], DIV2K validation [1] and a subset of our UH4K for quantitative evaluation while more datasets [2, 12, 25] for qualitative analysis.

### 4.4.1 Quantitative Results

Since PSNR and SSIM [44] have already been shown to correlate weakly with the human perception regarding image quality, we further utilize LPIPS [50] and PI [3] for evaluation. Following ESRGAN [42] and RankSRGAN [51] that provide different models for quantitative evaluation, we prepare two models, named Beby-GAN-PI and Beby-GAN. The former is obtained using similar approaches as ESRGAN-PI [42]. As shown in Table 2, GAN-based methods obtain better performance on perceptual metrics with lower PSNR/SSIM scores.

As for GAN-based methods, our Beby-GAN performs best on PSNR/SSIM measures. Also, our method yields new state-of-the-art in terms of LPIPS on all benchmark. In

Dataset	Metric	PSNR-Oriented Methods			GAN-Based Methods					
		SRResNet [20]	RRDB [42]	RCAN [52]	SRGAN [20]	ESRGAN-PI [42]	ESRGAN [42]	RankSRGAN [51] <sup>†</sup>	Beby-GAN-PI	Beby-GAN
Set14	LPIPS↓	0.3043	0.2934	0.2922	0.3162	0.2771	0.2372	0.2545	0.2537	<b>0.2202</b>
	PI↓	5.36	5.27	5.30	2.87	2.61	2.93	2.61	<b>2.57</b>	3.08
	PSNR↑	28.57	28.95	28.97	25.90	26.39	26.28	26.57	26.56	<b>26.96</b>
	SSIM↑	0.7834	0.7912	0.7913	0.6942	0.7021	0.6985	0.7052	0.7061	<b>0.7282</b>
BSDS100	LPIPS↓	0.3437	0.3341	0.3320	0.3387	0.2801	0.2599	0.2790	0.2777	<b>0.2385</b>
	PI↓	5.34	5.30	5.19	2.62	2.27	2.48	2.15	<b>2.13</b>	2.44
	PSNR↑	27.61	27.84	27.84	25.38	25.72	25.32	25.57	25.56	<b>25.81</b>
	SSIM↑	0.7376	0.7453	0.7456	0.6423	0.6638	0.6514	0.6492	0.6536	<b>0.6781</b>
DIV2K	LPIPS↓	0.2991	0.2863	0.2862	0.3109	0.2741	0.2222	0.2368	0.2352	<b>0.1991</b>
	PI↓	5.40	5.28	5.33	3.25	<b>2.95</b>	3.27	3.00	3.02	3.33
	PSNR↑	30.49	30.90	30.86	27.16	27.80	28.16	28.01	28.12	<b>28.71</b>
	SSIM↑	0.8391	0.8478	0.8469	0.7600	0.7653	0.7752	0.7652	0.7688	<b>0.7923</b>
UH4K	LPIPS↓	0.2304	0.2225	0.2208	0.3346	0.2694	0.2160	0.2745	0.2711	<b>0.2009</b>
	PI↓	5.53	5.50	5.56	3.91	2.93	3.42	<b>2.87</b>	2.89	3.54
	PSNR↑	32.11	32.45	32.46	27.85	28.94	29.43	28.99	29.13	<b>30.02</b>
	SSIM↑	0.8691	0.8756	0.8751	0.7706	0.7874	0.8052	0.7850	0.7892	<b>0.8214</b>

Table 2: Quantitative comparison of LPIPS [50], PI [3], PSNR and SSIM [44] on benchmarks. ‘↓’ means the lower, the better. ‘↑’ indicates the higher, the better. ‘†’ means that the results of RankSRGAN [51] are from multiple models optimized by different objectives. **Red: best** results in GAN-based methods.

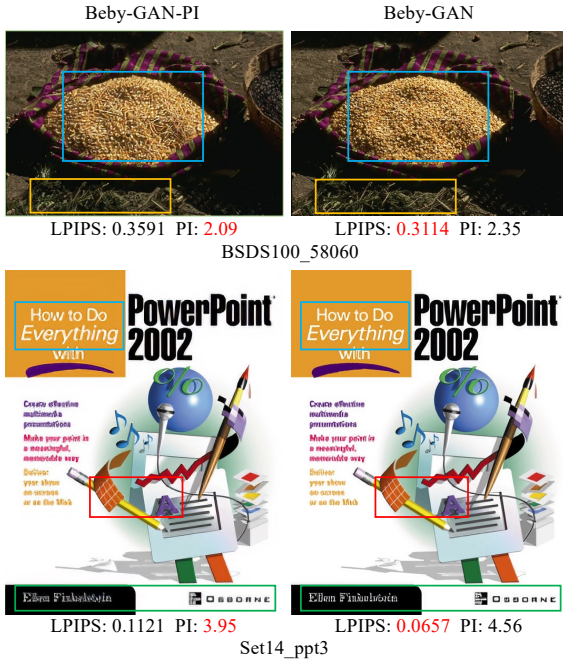


Figure 8: Comparison of Beby-GAN-PI and Beby-GAN. **Red: better** results. Ground-truth-based LPIPS is more representative and robust than no-reference-based PI. Zoom in for better visual comparison.

terms of PI, our PI-based model achieves superior performance on Set14 [49] and BSDS100 [23], as well as comparable results on DIV2K [1] and UH4K. We notice that there is a relatively large disparity between the ground-truth-based LPIPS and no-reference-based PI. As shown in Figure 8, LPIPS is more consistent with human perception. In this case, PI is only used for reference.

#### 4.4.2 Qualitative Results

As illustrated in Figure 10, PSNR-oriented methods (i.e., RRDB [42] and RCAN [52]) tend to generate overly-smooth results. Although existing GAN-based methods (i.e., ESRGAN [42] and RankSRGAN [51]) can recover some details, they possibly generate unpleasing visual artifacts (see UH4K\_020, DIV2K\_0823 and Set14\_Flowres) and color inconsistency (see Set14-Comic).

In contrast, our Beby-GAN is capable of producing more realistic results. From visualized examples in Figure 10, it is clear that our method reconstructs richer and more compelling patterns as well as sharper structures. Also, fewer artifacts are produced. In the following, we further present a comprehensive user study to evaluate the human visual quality of reconstructed images.

#### 4.5. User Study

In addition to our method, we take into consideration RCAN [52], ESRGAN [42] and RankSRGAN [51]. We prepare testing cases from three sources: (1) *Low-resolution images* stemming from the commonly used benchmark including Set5 [2], Set14 [49], BSDS100 [23] and Urban100 [12]. There are a total of 219 images. (2) *2K resolution images* from the validation subset of DIV2K [1]. 100 images are included. (3) *4K resolution images* in our UH4K dataset. There are over 400 images from 4 categories.

Every time we randomly display 30 testing cases and ask the participant to rank 4 versions of each image: RCAN, ESRGAN, RankSRGAN and our Beby-GAN. To make a fair comparison, we follow [51] to zoom in one small patch for each image.

We invite 30 participants to our user study. As shown



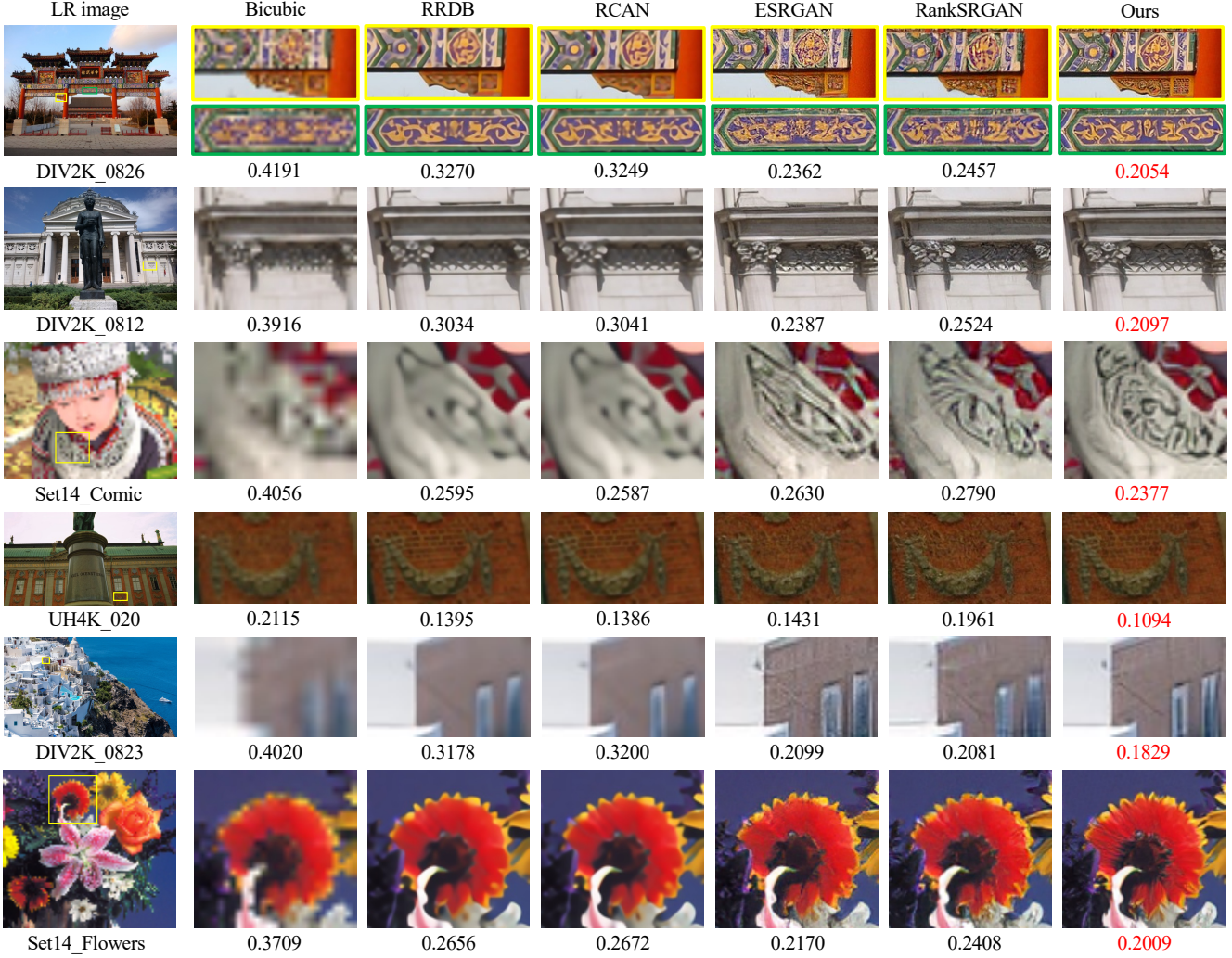


Figure 9: Visual comparison of our Beby-GAN with other methods on  $\times 4$  scale. The values beneath images represent LPIPS measures. **Red**: best quantitative results. It is clear that our Beby-GAN obtains the best visual performance.

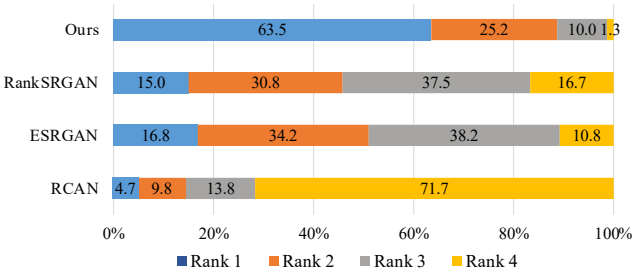


Figure 10: The ranking results of user study involving 30 participants. The values on the bars represent the percentages of rankings.

in the Figure 10, most of our results rank in the first place while the remaining of ours still gets high rankings. Especially, it is observed that our Beby-GAN outperforms others by a large margin on the 4K dataset from visual examples in

the appendix, generating more realistic details for this most challenging dataset. Besides, ESRGAN and RankSRGAN achieve better performance than RCAN. The user study not only demonstrates the superiority of our proposed Beby-GAN, but also explains that existing evaluation measures and human perception are diverse to some extent.

## 5. Conclusion

In this paper, we have presented best-buddy GANs (Beby-GAN) for highly detailed image super-resolution. By virtue of the proposed best-buddy loss and region-aware adversarial learning, our Beby-GAN is able to recover realistic texture while maintaining the naturalness of images. Extensive experiments along with the user study manifest the effectiveness of our method for SISR.

# Best-Buddy GANs for Highly Detailed Image Super-Resolution

## Appendix

Wenbo Li<sup>1\*</sup> Kun Zhou<sup>2\*</sup> Lu Qi<sup>1</sup> Liying Lu<sup>1</sup> Nianjuan Jiang<sup>2</sup> Jiangbo Lu<sup>2†</sup> Jiaya Jia<sup>1,2</sup>  
<sup>1</sup>The Chinese University of Hong Kong <sup>2</sup>Smartmore Corporation

### 1. Additional Qualitative Results

Here we present more visual examples on our proposed ultra-high resolution 4K (UH4K), DIV2K [1] and BSDS100 [23] datasets, as shown in Figure 1, 2, 3, 4, 5, 6. Compared with SRResNet [20], RRDB [42], RCAN [52], SRGAN [20], ESRGAN [42] and RankSRGAN [51], our

best-buddy GANs (Beby-GAN) recovers more realistic texture while maintaining the naturalness of images. Especially, it is observed that our Beby-GAN recovers more regular structures and richer details on the UH4K dataset, achieving higher perceptual quality. We also show a demo video, which compares the results of our Beby-GAN and bicubic-upsampled (BI) results.

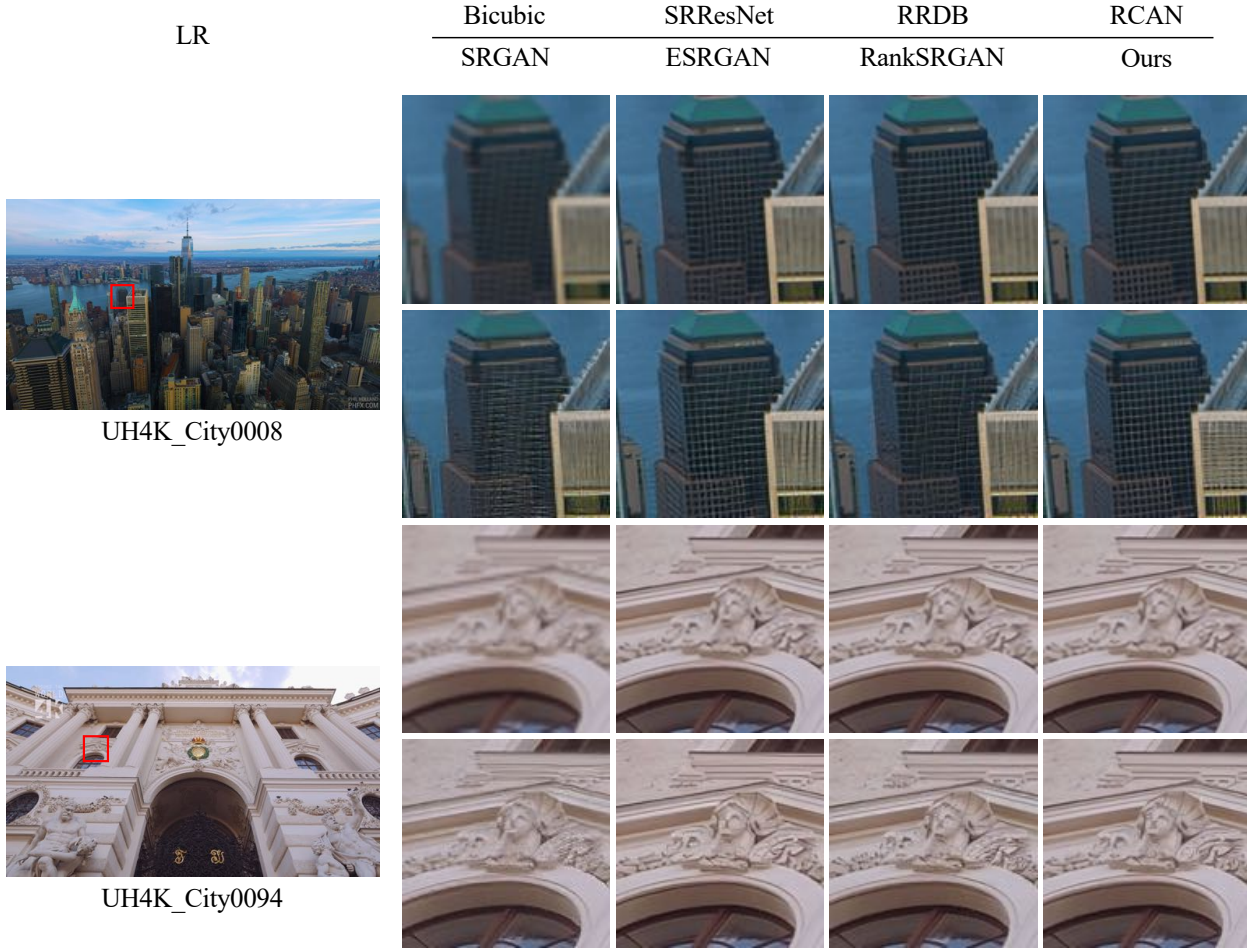


Figure 1: Visual comparison of our Beby-GAN with other methods on  $\times 4$  scale (part 1).



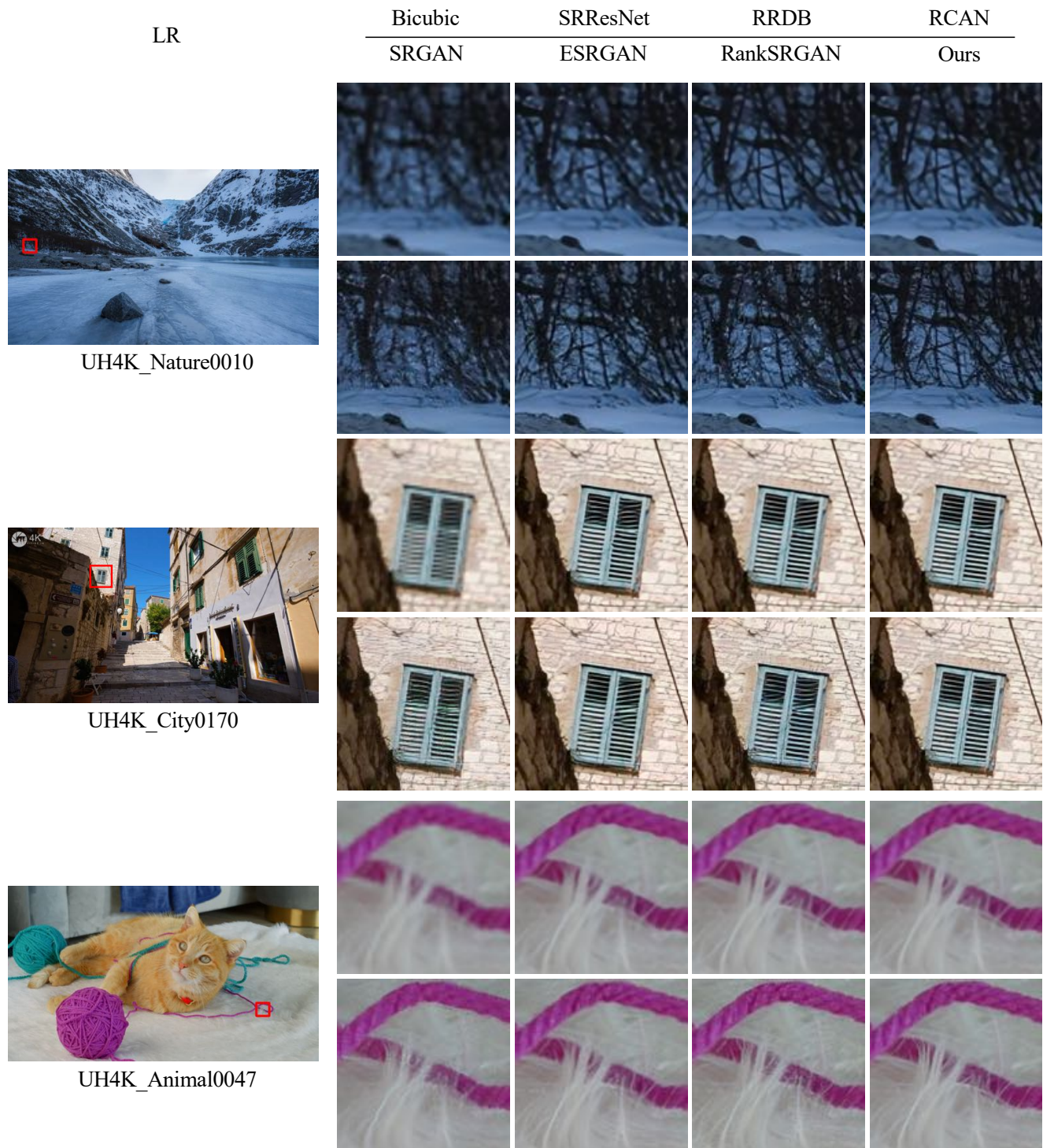


Figure 2: Visual comparison of our Beby-GAN with other methods on  $\times 4$  scale (part 2).



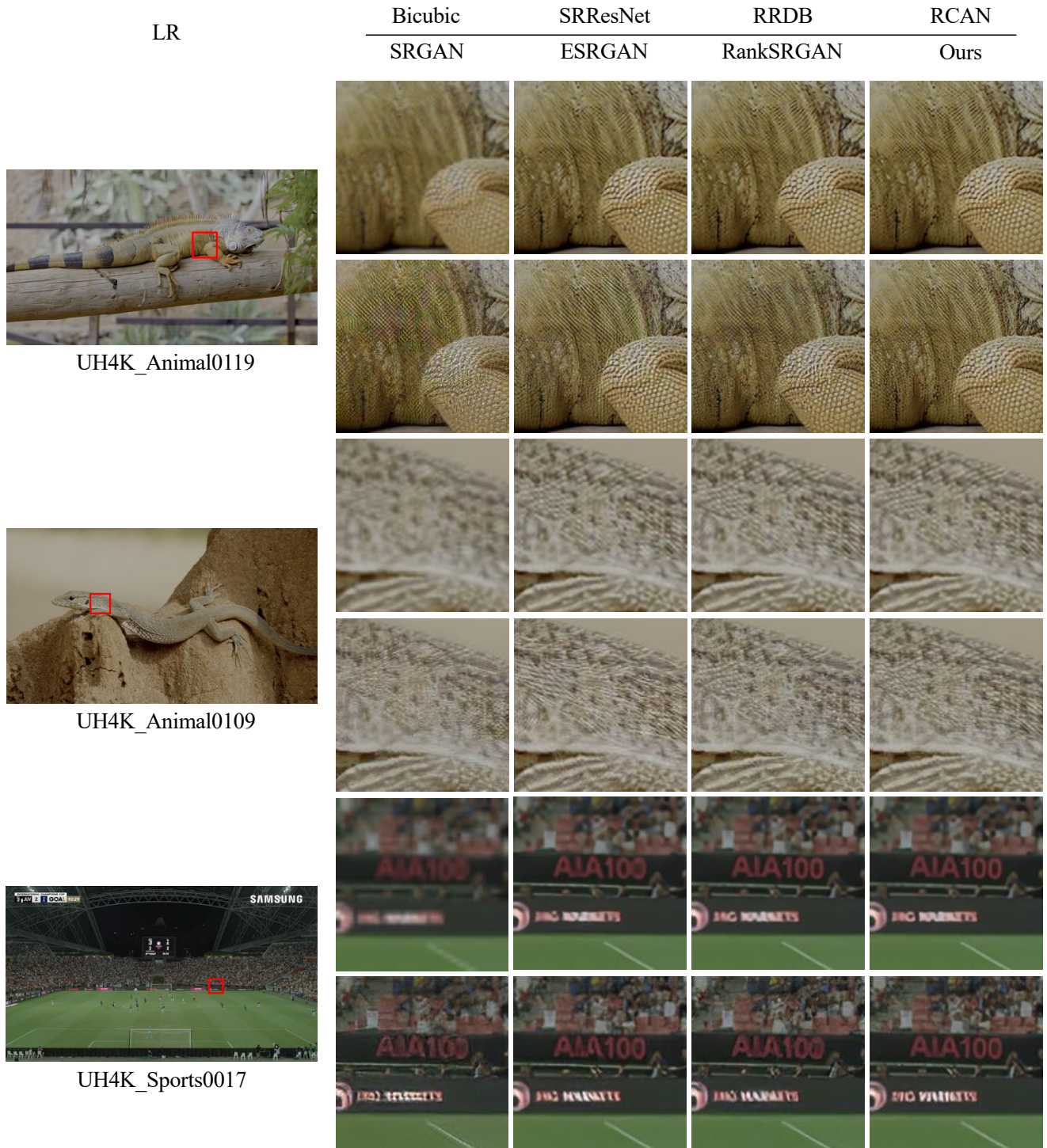


Figure 3: Visual comparison of our Beby-GAN with other methods on  $\times 4$  scale (part 3).

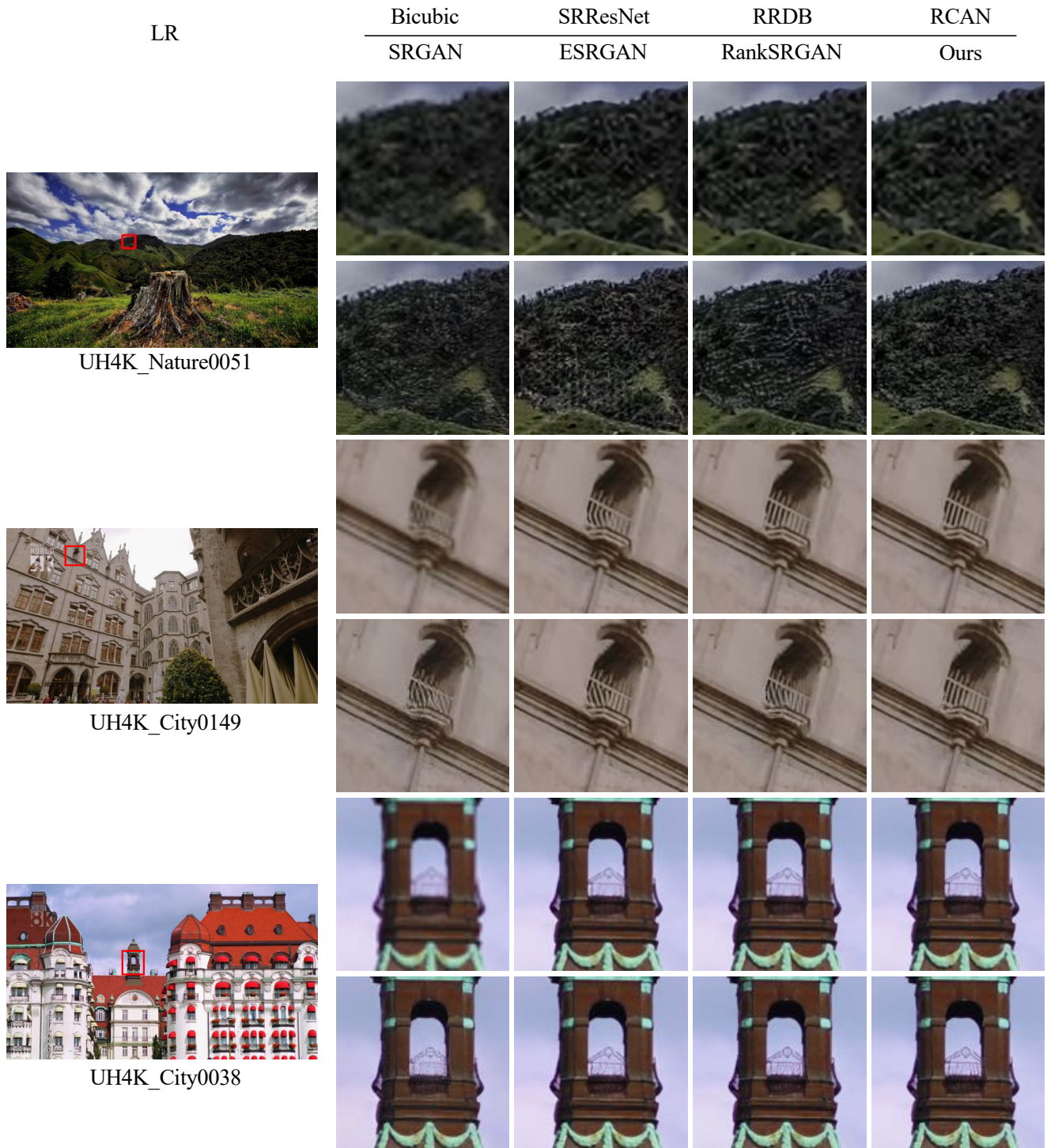


Figure 4: Visual comparison of our Beby-GAN with other methods on  $\times 4$  scale (part 4).



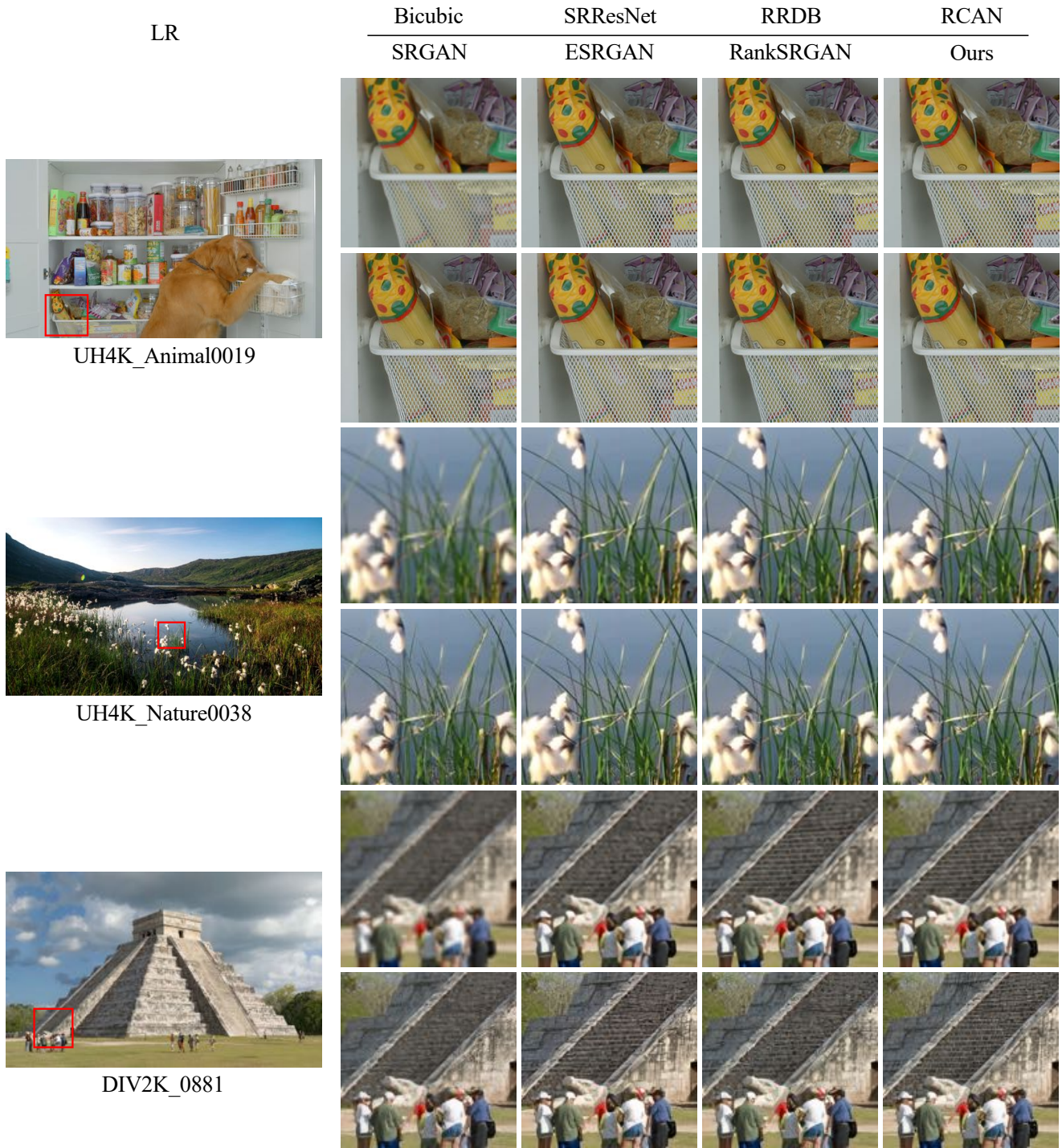


Figure 5: Visual comparison of our Beby-GAN with other methods on  $\times 4$  scale (part 5).



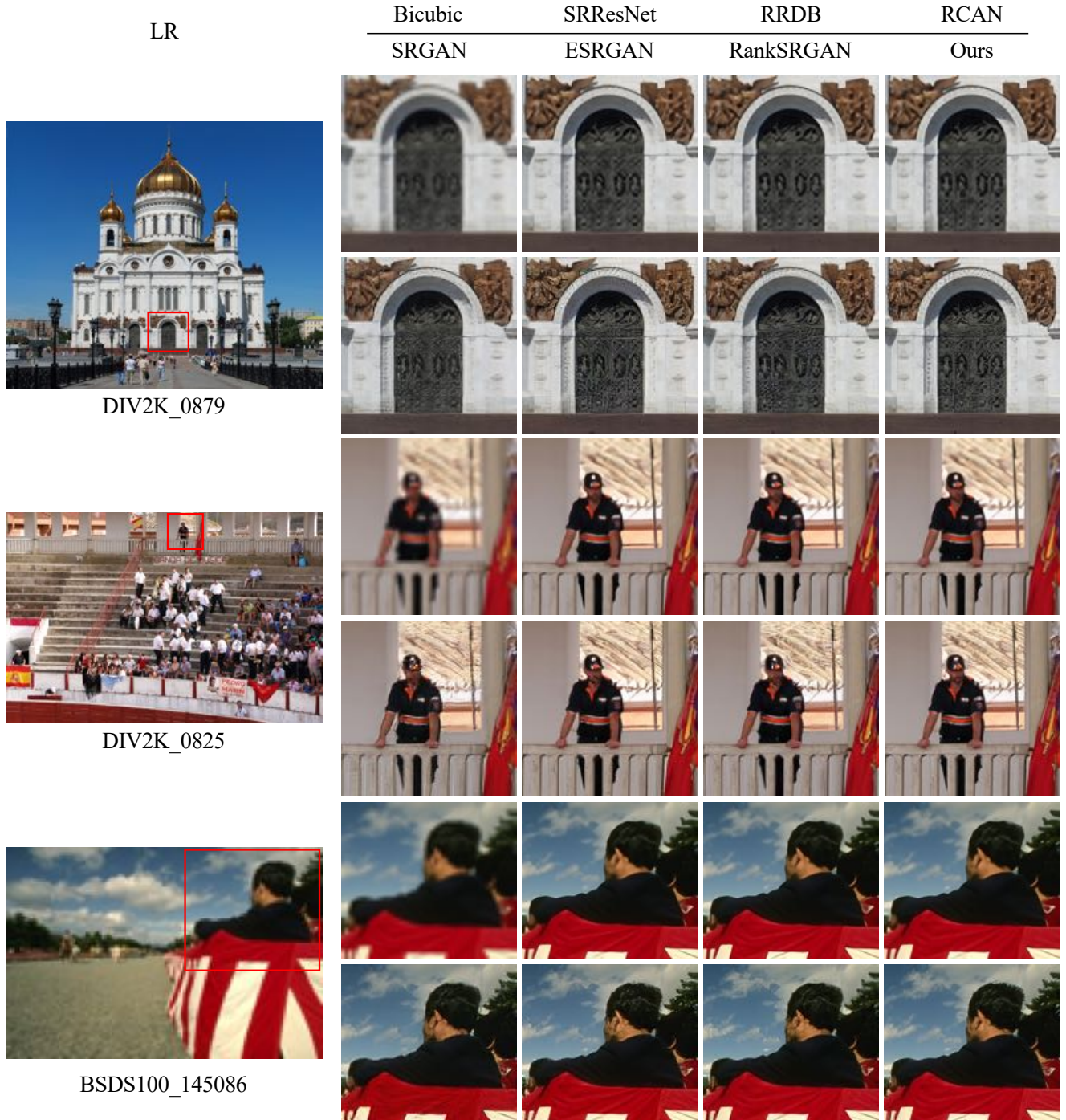


Figure 6: Visual comparison of our Beby-GAN with other methods on  $\times 4$  scale (part 6).

## 2. Masked HR Images



Figure 7: Visual examples of masked HR images (part 1).

In Sec. 3.2, we describe a region-aware adversarial learning strategy, where a mask is introduced to differentiate the rich-texture areas from smooth ones for each image. The mask is obtained from a ground-truth HR image based on Eq. 5. Here, we show more visual examples of HR images and the corresponding masked results in Figure 7, 8, 9. The smooth regions are masked with the black color while the rich-texture areas are preserved. It is clear that our method could separate the rich-texture and smooth regions. Though more sophisticated strategies can be used at the cost of more

computation, we have demonstrated that this simple masking method already works very well, as detailed in the ablation study section.



HR Image



Masked HR Image

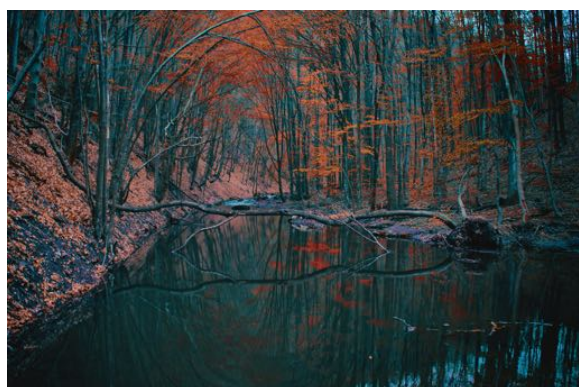


Figure 8: Visual examples of masked HR images (part 2).



HR Image



Masked HR Image

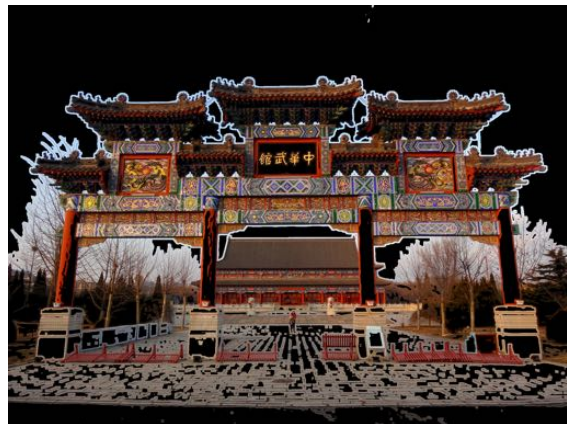


Figure 9: Visual examples of masked HR images (part 3).

### 3. Supplementary Results of Sect. 4.4

Apart from LPIPS [50], PI [3], PSNR and SSIM [44] results shown in Sect. 4.4, we also report the NIQE [27] performance of our Beby-GAN-PI and Beby-GAN models in Table 1. Besides, as shown in Figure 10, we add the ground-truth images to the visual comparison figure in Sect. 4.4 for a better comparison.

Datasets	Set14	BSDS100	DIV2K	UH4K
Beby-GAN-PI	3.21	2.98	2.73	2.46
Beby-GAN	4.09	3.53	3.21	3.40

Table 1: NIQE results of Beby-GAN-PI and Beby-GAN.

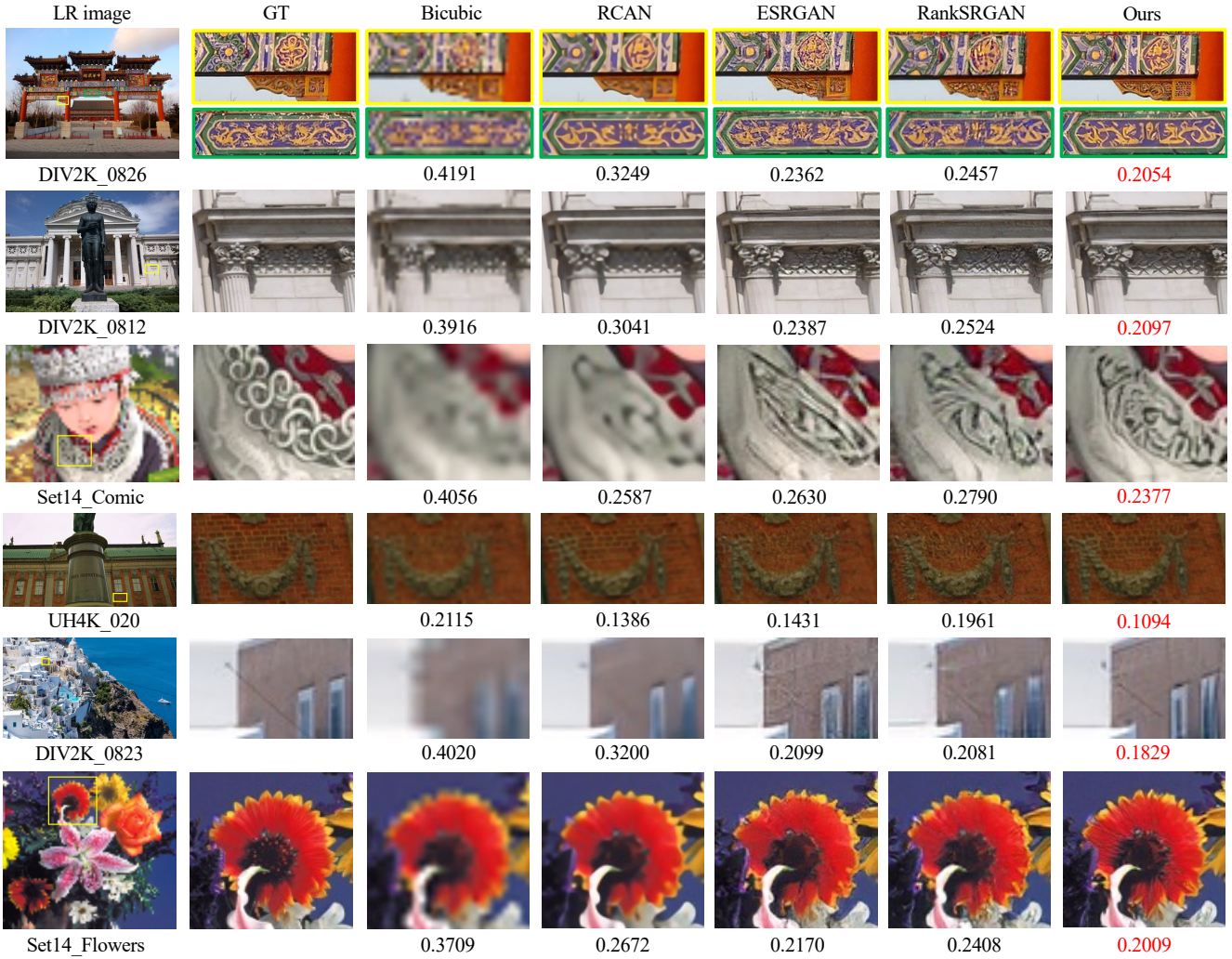


Figure 10: Visual comparison of our Beby-GAN with other methods on  $\times 4$  scale. The values beneath images represent LPIPS measures. **Red**: best quantitative results. It is clear that our method obtains the best visual performance.

### References

- [1] Eirikur Agustsson and Radu Timofte. Ntire 2017 challenge on single image super-resolution: Dataset and study. In *CVPRW*, pages 126–135, 2017. **5, 6, 7, 9**
- [2] Marco Bevilacqua, Aline Roumy, Christine Guillemot, and Marie Line Alberi-Morel. Low-complexity single-image super-resolution based on nonnegative neighbor embedding. 2012. **5, 6, 7**
- [3] Yochai Blau, Roey Mechrez, Radu Timofte, Tomer Michaeli, and Lihi Zelnik-Manor. The 2018 pirm challenge on perceptual image super-resolution. In *ECCV*, pages 0–0, 2018. **5, 6, 7, 18**
- [4] Chao Dong, Chen Change Loy, Kaiming He, and Xiaoou Tang. Learning a deep convolutional network for image super-resolution. In *ECCV*, pages 184–199. Springer, 2014.



1, 2

- [5] Alexey Dosovitskiy and Thomas Brox. Generating images with perceptual similarity metrics based on deep networks. In *NIPS*, pages 658–666, 2016. 3, 5
- [6] Joan Bruna Estrach, Pablo Sprechmann, and Yann LeCun. Super-resolution with deep convolutional sufficient statistics. In *ICLR*, 2016. 3, 5
- [7] Manuel Fritsche, Shuhang Gu, and Radu Timofte. Frequency separation for real-world super-resolution. In *ICCVW*, pages 3599–3608. IEEE, 2019. 2
- [8] Daniel Glasner, Shai Bagon, and Michal Irani. Super-resolution from a single image. In *ICCV*, pages 349–356. IEEE, 2009. 1, 2, 4
- [9] Ian Goodfellow, Jean Pouget-Abadie, Mehdi Mirza, Bing Xu, David Warde-Farley, Sherjil Ozair, Aaron Courville, and Yoshua Bengio. Generative adversarial nets. In *NIPS*, pages 2672–2680, 2014. 1, 3
- [10] Muhammad Haris, Gregory Shakhnarovich, and Norimichi Ukita. Deep back-projection networks for super-resolution. In *CVPR*, pages 1664–1673, 2018. 1, 2
- [11] Xuecai Hu, Haoyuan Mu, Xiangyu Zhang, Zilei Wang, Tieniu Tan, and Jian Sun. Meta-sr: A magnification-arbitrary network for super-resolution. In *CVPR*, pages 1575–1584, 2019. 2
- [12] Jia-Bin Huang, Abhishek Singh, and Narendra Ahuja. Single image super-resolution from transformed self-exemplars. In *CVPR*, pages 5197–5206, 2015. 1, 4, 5, 6, 7
- [13] Shady Abu Hussein, Tom Tirer, and Raja Giryes. Correction filter for single image super-resolution: Robustifying off-the-shelf deep super-resolvers. In *CVPR*, pages 1428–1437, 2020. 2
- [14] Justin Johnson, Alexandre Alahi, and Li Fei-Fei. Perceptual losses for real-time style transfer and super-resolution. In *ECCV*, pages 694–711. Springer, 2016. 1, 2, 3, 5
- [15] Alexia Jolicoeur-Martineau. The relativistic discriminator: a key element missing from standard gan. *arXiv preprint arXiv:1807.00734*, 2018. 5
- [16] Jiwon Kim, Jung Kwon Lee, and Kyoung Mu Lee. Accurate image super-resolution using very deep convolutional networks. In *CVPR*, pages 1646–1654, 2016. 1, 2
- [17] Jiwon Kim, Jung Kwon Lee, and Kyoung Mu Lee. Deeply-recursive convolutional network for image super-resolution. In *CVPR*, pages 1637–1645, 2016. 1, 2
- [18] Stefan Kindermann, Stanley Osher, and Peter W Jones. Deblurring and denoising of images by nonlocal functionals. *Multiscale Modeling & Simulation*, 4(4):1091–1115, 2005. 4
- [19] Wei-Sheng Lai, Jia-Bin Huang, Narendra Ahuja, and Ming-Hsuan Yang. Deep laplacian pyramid networks for fast and accurate super-resolution. In *CVPR*, pages 624–632, 2017. 1, 2
- [20] Christian Ledig, Lucas Theis, Ferenc Huszár, Jose Caballero, Andrew Cunningham, Alejandro Acosta, Andrew Aitken, Alykhan Tejani, Johannes Totz, Zehan Wang, et al. Photo-realistic single image super-resolution using a generative adversarial network. In *CVPR*, pages 4681–4690, 2017. 1, 2, 3, 6, 7, 9
- [21] Wenbo Li, Xin Tao, Taian Guo, Lu Qi, Jiangbo Lu, and Ji-aya Jia. Mucan: Multi-correspondence aggregation network for video super-resolution. *arXiv preprint arXiv:2007.11803*, 2020. 4
- [22] Bee Lim, Sanghyun Son, Heewon Kim, Seungjun Nah, and Kyoung Mu Lee. Enhanced deep residual networks for single image super-resolution. In *CVPRW*, pages 136–144, 2017. 1, 2
- [23] David Martin, Charless Fowlkes, Doron Tal, and Jitendra Malik. A database of human segmented natural images and its application to evaluating segmentation algorithms and measuring ecological statistics. In *ICCV*, volume 2, pages 416–423. IEEE, 2001. 1, 5, 6, 7, 9
- [24] Michael Mathieu, Camille Couprie, and Yann LeCun. Deep multi-scale video prediction beyond mean square error. In *ICLR*, 2016. 3
- [25] Yusuke Matsui, Kota Ito, Yuji Aramaki, Azuma Fujimoto, Toru Ogawa, Toshihiko Yamasaki, and Kiyoharu Aizawa. Sketch-based manga retrieval using manga109 dataset. *Multimedia Tools and Applications*, 76(20):21811–21838, 2017. 6
- [26] Roey Mechrez, Itamar Talmi, Firas Shama, and Lihi Zelnik-Manor. Maintaining natural image statistics with the contextual loss. In *ACCV*, pages 427–443. Springer, 2018. 1, 2
- [27] Anish Mittal, Rajiv Soundararajan, and Alan C Bovik. Making a “completely blind” image quality analyzer. *SPL*, 20(3):209–212, 2012. 18
- [28] Tomer Peleg and Michael Elad. A statistical prediction model based on sparse representations for single image super-resolution. *TIP*, 23(6):2569–2582, 2014. 1, 2
- [29] Matan Protter, Michael Elad, Hiroyuki Takeda, and Peyman Milanfar. Generalizing the nonlocal-means to super-resolution reconstruction. *TIP*, 18(1):36–51, 2008. 1, 4
- [30] Yaniv Romano, Matan Protter, and Michael Elad. Single image interpolation via adaptive nonlocal sparsity-based modeling. *TIP*, 23(7):3085–3098, 2014. 1, 2
- [31] Mehdi SM Sajjadi, Bernhard Scholkopf, and Michael Hirsch. Enhancenet: Single image super-resolution through automated texture synthesis. In *ICCV*, pages 4491–4500, 2017. 2, 3
- [32] Wenzhe Shi, Jose Caballero, Ferenc Huszár, Johannes Totz, Andrew P Aitken, Rob Bishop, Daniel Rueckert, and Zehan Wang. Real-time single image and video super-resolution using an efficient sub-pixel convolutional neural network. In *CVPR*, pages 1874–1883, 2016. 1, 2
- [33] Karen Simonyan and Andrew Zisserman. Very deep convolutional networks for large-scale image recognition. In *ICLR*, 2015. 5
- [34] Jae Woong Soh, Gu Yong Park, Junho Jo, and Nam Ik Cho. Natural and realistic single image super-resolution with explicit natural manifold discrimination. In *CVPR*, pages 8122–8131, 2019. 1, 2, 3, 5
- [35] Casper Kaae Sønderby, Jose Caballero, Lucas Theis, Wenzhe Shi, and Ferenc Huszár. Amortised map inference for image super-resolution. *arXiv preprint arXiv:1610.04490*, 2016. 1, 2

- [36] Ying Tai, Jian Yang, and Xiaoming Liu. Image super-resolution via deep recursive residual network. In *CVPR*, pages 3147–3155, 2017. 1, 2
- [37] Ying Tai, Jian Yang, Xiaoming Liu, and Chunyan Xu. Memnet: A persistent memory network for image restoration. In *ICCV*, pages 4539–4547, 2017. 1, 2
- [38] Radu Timofte, Eirikur Agustsson, Luc Van Gool, Ming-Hsuan Yang, and Lei Zhang. Ntire 2017 challenge on single image super-resolution: Methods and results. In *CVPRW*, pages 114–125, 2017. 5
- [39] Radu Timofte, Vincent De Smet, and Luc Van Gool. Anchored neighborhood regression for fast example-based super-resolution. In *ICCV*, pages 1920–1927, 2013. 1, 2
- [40] Radu Timofte, Vincent De Smet, and Luc Van Gool. A+: Adjusted anchored neighborhood regression for fast super-resolution. In *Asian conference on computer vision*, pages 111–126. Springer, 2014. 2
- [41] Xintao Wang, Ke Yu, Chao Dong, and Chen Change Loy. Recovering realistic texture in image super-resolution by deep spatial feature transform. In *CVPR*, pages 606–615, 2018. 2
- [42] Xintao Wang, Ke Yu, Shixiang Wu, Jinjin Gu, Yihao Liu, Chao Dong, Yu Qiao, and Chen Change Loy. Esrgan: Enhanced super-resolution generative adversarial networks. In *ECCV*, pages 0–0, 2018. 1, 2, 3, 5, 6, 7, 9
- [43] Yifan Wang, Federico Perazzi, Brian McWilliams, Alexander Sorkine-Hornung, Olga Sorkine-Hornung, and Christopher Schroers. A fully progressive approach to single-image super-resolution. In *CVPRW*, pages 864–873, 2018. 2
- [44] Zhou Wang, Alan C Bovik, Hamid R Sheikh, and Eero P Simoncelli. Image quality assessment: from error visibility to structural similarity. *TIP*, 13(4):600–612, 2004. 5, 6, 7, 18
- [45] Chih-Yuan Yang, Jia-Bin Huang, and Ming-Hsuan Yang. Exploiting self-similarities for single frame super-resolution. In *ACCV*, pages 497–510. Springer, 2010. 1, 2, 4
- [46] Jianchao Yang, Zhaowen Wang, Zhe Lin, Scott Cohen, and Thomas Huang. Coupled dictionary training for image super-resolution. *IEEE transactions on image processing*, 21(8):3467–3478, 2012. 2
- [47] Jianchao Yang, John Wright, Thomas Huang, and Yi Ma. Image super-resolution as sparse representation of raw image patches. In *CVPR*, pages 1–8. IEEE, 2008. 1, 2
- [48] Jianchao Yang, John Wright, Thomas S Huang, and Yi Ma. Image super-resolution via sparse representation. *TIP*, 19(11):2861–2873, 2010. 1
- [49] Roman Zeyde, Michael Elad, and Matan Protter. On single image scale-up using sparse-representations. In *International conference on curves and surfaces*, pages 711–730. Springer, 2010. 1, 2, 5, 6, 7
- [50] Richard Zhang, Phillip Isola, Alexei A Efros, Eli Shechtman, and Oliver Wang. The unreasonable effectiveness of deep features as a perceptual metric. In *Proceedings of the IEEE conference on computer vision and pattern recognition*, pages 586–595, 2018. 5, 6, 7, 18
- [51] Wenlong Zhang, Yihao Liu, Chao Dong, and Yu Qiao. Ranksgan: Generative adversarial networks with ranker for image super-resolution. In *ICCV*, pages 3096–3105, 2019. 1, 2, 3, 5, 6, 7, 9
- [52] Yulun Zhang, Kunpeng Li, Kai Li, Lichen Wang, Bineng Zhong, and Yun Fu. Image super-resolution using very deep residual channel attention networks. In *ECCV*, pages 286–301, 2018. 1, 2, 6, 7, 9
- [53] Yulun Zhang, Yapeng Tian, Yu Kong, Bineng Zhong, and Yun Fu. Residual dense network for image super-resolution. In *CVPR*, pages 2472–2481, 2018. 1, 2